www.acsnano.org

Bright Silicon Nanocrystals from a Liquid Precursor: Quasi-Direct Recombination with **High Quantum Yield**

Todd A. Pringle,* Katharine I. Hunter, Alexandra Brumberg, Kenneth J. Anderson, Jeffrey A. Fagan, Salim A. Thomas, Reed J. Petersen, Mahmud Sefannaser, Yulun Han, Samuel L. Brown, Dmitri S. Kilin, Richard D. Schaller, Uwe R. Kortshagen, Philip Raymond Boudjouk, and Erik K. Hobbie*



Downloaded via NORTH DAKOTA STATE UNIV on July 1, 2021 at 07:43:30 (UTC). See https://pubs.acs.org/sharingguidelines for options on how to legitimately share published articles.

Cite This: ACS Nano 2020, 14, 3858-3867



Read Online

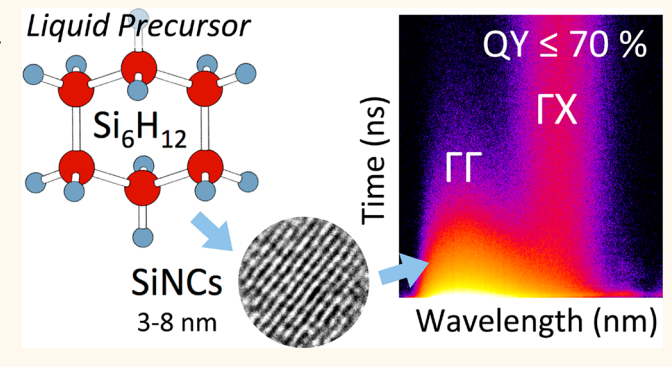
ACCESS

III Metrics & More

Article Recommendations

Supporting Information

ABSTRACT: Silicon nanocrystals (SiNCs) with bright bandgap photoluminescence (PL) are of current interest for a range of potential applications, from solar windows to biomedical contrast agents. Here, we use the liquid precursor cyclohexasilane (Si₆H₁₂) for the plasma synthesis of colloidal SiNCs with exemplary core emission. Through size separation executed in an oxygen-shielded environment, we achieve PL quantum yields (QYs) approaching 70% while exposing intrinsic constraints on efficient core emission from smaller SiNCs. Time-resolved PL spectra of these fractions in response to femtosecond pulsed excitation reveal a zero-phonon radiative channel that anticorrelates with QY, which we model using advanced computational methods applied to a 2 nm SiNC. Our



results offer additional insight into the photophysical interplay of the nanocrystal surface, quasi-direct recombination, and efficient SiNC core PL.

KEYWORDS: silicon nanocrystals, liquid silane, photoluminescence quantum yield, quantum confinement, surface effects

remiconductor nanocrystals are the focus of a tremendous amount of research directed at a broad range of potential applications, from photovoltaics and fluorescent contrast agents to color displays such as the recently commercialized QLED television. While the main effort continues to be directed at achieving bright tunable photoluminescence (PL) from solution-processed direct-bandgap materials (e.g., cadmium selenide, indium phosphide, and leadhalide perovskites), niche applications such as biolabeling and light harvesting are often better served by nontoxic materials that possess a significant Stokes shift, and in this regard colloidal silicon nanocrystals (SiNCs) remain an intriguing material of potential relevance. 1,2

The PL from the SiNC core is strongly influenced by the indirect nature of the fundamental bandgap, 3-6 with large Stokes shifts, broad PL line widths, and long PL lifetimes-up to hundreds of microseconds-with a broad distribution of decay rates.^{7–11} Beyond this simple view, there are a number of unresolved questions related to the interplay of surface effects and quantum confinement, 12,13 intrinsic limits on core emission and PL quantum yield (QY),14 the nature of electron-phonon coupling, 15 and interaction effects in SiNC solids and composites. $^{16-20}$ Of particular note is the observation that steady-state PL from the nanocrystal core is never observed at emission energies above the yellow, 14 which puts significant constraints on potential applications. At the same time, several recent studies have reported multimodal PL relaxation spanning a range of wavelengths and time scales, 21-25 where the faster modes have been attributed to both surface effects and quasi-direct recombination, 26-35 although the distinction between the two is becoming increasingly blurred. In studies directed at extending the range of visible SiNC luminescence to shorter wavelengths, recent focus has been on bright size-independent emission tuned through a variety of complex surface ligands, 36-39 with

Received: December 8, 2019 Accepted: March 9, 2020 Published: March 9, 2020





the primary role of the Si core being optical absorption, and where PL color is determined by the charge-transfer characteristics of the ligands as opposed to quantum confinement.

Synthetically, there are several routes to colloidal SiNCs, \$^{40-45}\$ but the approach of interest here is the nonthermal plasma method. \$^{46-4749}\$ From a typical precursor such as monosilane gas (SiH4), lab-scale plasma reactors provide good yield \$^{50}\$ with bright PL. \$^{51,52}\$ The plasma approach can also accommodate chemical doping \$^{53,54}\$ and core—shell architectures \$^{55}\$ as well as unique surface chemistries. \$^{56}\$ While the typical precursor for the nonthermal plasma method is silane gas, liquid silanes \$^{57}\$ represent intriguing alternatives, both from the perspective of safety and, potentially, increased SiNC mass yield. The liquid silane precursor of interest here, cyclohexasilane (CHS), was selected because of its availability at North Dakota State University (NDSU) as well as our familiarity with using it for material synthesis. \$^{58-60}\$ While still pyrophoric, liquid CHS is much less dangerous than silane gas.

In this contribution, we present a comprehensive study of SiNC photophysics specifically directed at addressing many of the longstanding questions touched on above. In doing so, we demonstrate liquid CHS as a viable precursor for the plasma synthesis of SiNCs that exhibit bright core PL, with parent alkene-passivated suspensions exhibiting PL maxima in the range of 700-1000 nm and QYs approaching 60%. Using density-gradient ultracentrifugation (DGU) executed in an oxygen-shielded environment, we further process these SiNCs into size-resolved fractions with QYs approaching 70%, where these fractions are "pristine" in the sense that they have been shielded from ambient atmospheric conditions. Time-resolved PL spectra of these fractions in response to pulsed excitation with lifetimes spanning 100 ps to hundreds of µs-suggest a quasi-direct radiative channel that correlates with lower OY, which we model using advanced computational methods applied to a 2 nm SiNC. Our results offer additional insight into the photophysical interplay of the nanocrystal surface, quasi-direct recombination, and bright core PL, while explaining the absence of efficient core PL from smaller SiNCs.

RESULTS AND DISCUSSION

The precursor (CHS) was synthesized as detailed in Materials and Methods, and SiNCs were synthesized from CHS in a nonthermal plasma reactor at NDSU (Materials and Methods). The SiNCs were thermally passivated for at least 3 h with 1-dodecene in mesitylene at 185 °C to impart colloidal stability and optimize PL, with 1-hexene and dodecene/hexene mixtures giving comparable results (data not presented). All steps were carried out in a nitrogen-filled glovebox. Figure 1a shows a schematic of the process. FTIR spectra were used to confirm hydrogen surface passivation in the dry reactant (Figure 1b), which is important for achieving high QY. 47-52 A spectral analysis of the SiH_x peaks and full FTIR spectra for a dry reactant and colloid corresponding to optimal PL QY are shown in the Supporting Information (Figure S1), along with additional FTIR, X-ray photoelectron spectroscopy (XPS), and thermogravimetric (TGA) analysis. Both XRD and Raman spectroscopy confirm SiNC crystallinity (Figure 1c,d), also evident in TEM (inset, Figure 1c). The SiNCs produced in this study are 3-8 nm in diameter, with a step-like asymmetry emerging in the Raman spectra for smaller SiNCs (Figure 1d). 15 Typical size distributions for parent SiNC suspensions obtained using transmission electron

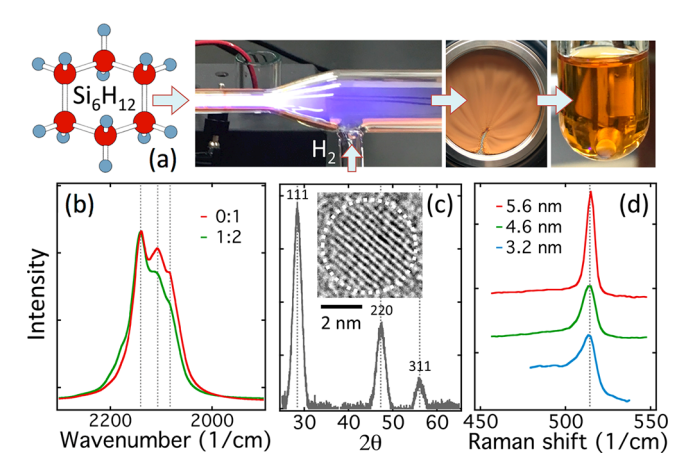


Figure 1. (a) Schematic of SiNC synthesis: Chemical structure of CHS, the plasma reactor, the raw product, and the passivated colloid. (b) Plot of the $\mathrm{SiH_x}$ FTIR peaks (vertical dashed lines) for ratios of 0:1 (red) and 1:2 (green) carrier gas to injected hydrogen. (c) XRD curves for a dried SiNC colloid (860 nm PL peak, 53% QY) with a TEM image of an individual SiNC. (d) Raman spectra of three dried colloidal SiNC samples (with diameter estimated from the PL peak) spanning the window of measured emission.

microscopy (TEM) can be found in the Supporting Information (Figure S2).

Bandgap Photoluminescence. Parent SiNC suspensions were shielded from atmospheric oxygen throughout the synthesis—passivation—characterization sequence, with typical PL spectra shown in Figure 2a. Quantum confinement leads to a 250 nm variation in PL peak across the window of nanocrystal sizes studied. In contrast, the absorption spectra show little size dependence (Figure 2b), with absorption

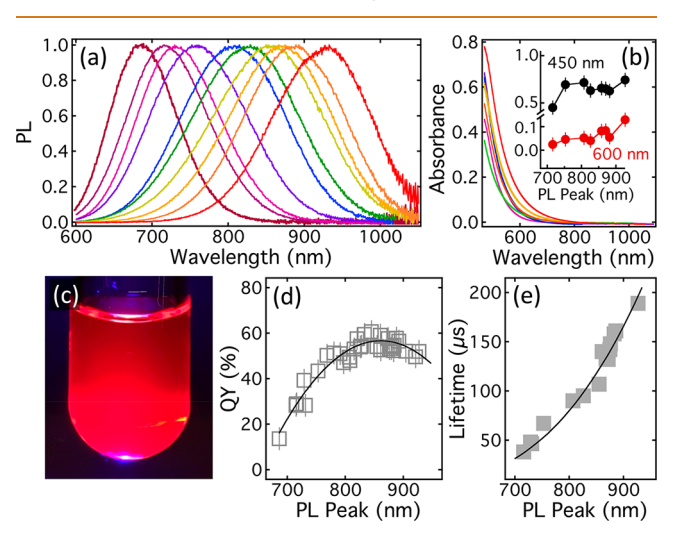


Figure 2. (a) Representative PL spectra of different parent SiNC suspensions in mesitylene immediately after passivation with 1-dodecene and without exposure to air. (b) Normalized absorption spectra for some of the samples depicted in panel (a). The inset shows the absorption at 600 nm (red) and 450 nm (black) as a function of PL peak wavelength. (c) Stable red PL from a colloid after passivation. (d) QY as a function of PL peak for representative parent samples with a third-order polynomial fit. (e) PL lifetime *versus* peak emission wavelength and with the exponential fit detailed in the text. Excitation wavelength in panels (a), (c), (d), and (e) was 375 nm.

ACS Nano www.acsnano.org

occurring predominantly at the direct optical transitions of silicon¹² with a large size-dependent Stokes shift. The brightest emission extends well into the red (Figure 2c), approaching the near-infrared (NIR), with the PL QY exhibiting a maximum of 60% near an emission peak of 850 nm (Figure 2d). These QY values are comparable to the best values in the literature for core PL from SiNCs, demonstrating CHS as an attractive precursor for SiNC synthesis. 50-515

PL relaxation follows a stretched exponential decay, as detailed in the Supporting Information (Figure S3). This is indicative of a broad distribution of PL relaxation rates that varies with emission energy/wavelength.^{8,61} As shown in Figure 2e, the PL lifetimes of the parent suspensions range from 30 to 200 µs with increasing NC size or decreasing bandgap (E_{σ}) . The PL lifetime, τ , scales as $\exp(-E/E_0)$, where E is the emission peak energy and E_0 is a reference energy scale $(E_0 = 0.24 \text{ eV for the fit shown in Figure 2e})^{.5,62}$ The physical picture is one of "hot" electrons created through the absorption of blue/UV light at the direct ($\Gamma\Gamma$) optical transitions that then thermalize to states near the top of the band edge (ΓX) , where they wait for phonons with suitable momentum shift for radiative recombination. Electronphonon coupling is thus the root cause of both long lifetime and broad line width for size monodisperse SiNCs, as described elsewhere.8,25

Density Gradient Ultracentrifugation. Having demonstrated CHS as a viable precursor for the production of brightly luminescent SiNCs, we look for additional insight into the fundamental photophysics. To do so, we separate the SiNCs into size-resolved fractions using density gradient ultracentrifugation $(DGU)^{63-65}$ in chloroform/m-xylene mixtures, where details of the approach can be found in the Supporting Information. Exposure of the suspensions to ambient oxygen immediately leads to a drop in QY, while also potentially contributing to the slow growth of an oxide shell. While the former can be reversible,66 the latter leads to an irreversible blueshift in PL, which can complicate relating SiNC size to emission peak. Hence, all solvents were sparged with N2 prior to use, and the entire process of creating the gradient, loading the parent, spinning the parent, and robotically extracting the fractions (as well as long-term storage) was carried out in a manner that shielded the SiNCs from ambient conditions. SiNC sizes were extracted with TEM once all optical measurements were complete, with size distributions for typical fractions provided in the Supporting Information (Figure S4).

Figure 3 highlights typical fractions obtained through our process, where the PL peak and QY for the parent are indicated as a horizontal dashed line in Figure 3b,c. The fraction number can be converted to depth in the centrifuge tube through multiplication by 2 mm. The shaded region in Figure 3c is the absorption measured in an integrating sphere, which we use as an approximate measure of concentration. The increase in QY with respect to the parent can be explained by the removal of non-emitting impurities, such as SiNC aggregates, as well as a reduction in polydispersity due to the fact that QY is so strongly dependent on size. Note that the PL line widths in Figure 3a are reduced compared to the parents (30-35% for a parent with a PL peak near 850 nm) but are still large compared to direct-bandgap nanocrystals. The polydispersity index of the fractions, defined as $1 + \langle \delta R^2 \rangle /$ $\langle R \rangle^2$, where R is the SiNC radius and δR is the deviation from the mean, ranges from ≤1.01 (parent PL peak <900 nm) to

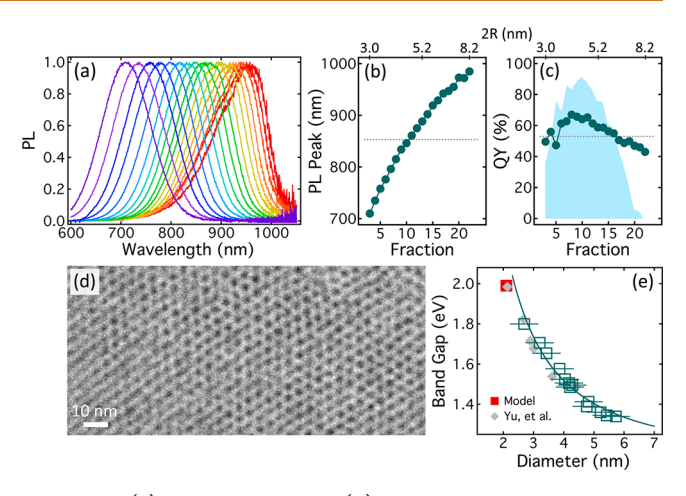


Figure 3. (a) PL spectra and (b) PL peak wavelength versus fraction number (equivalent to depth in the centrifuge tube measured in units of 2 mm) for DGU fractions obtained from a parent SiNC suspension with a PL peak of 853 nm and a QY of 53%. (c) QY versus fraction number for the fractions in (a) and (b). The shaded background indicates the absorption ("mass") of each fraction in arbitrary units. (d) TEM image of a SiNC superlattice from a DGU fraction (PL peak = 816 nm, QY = 68%) of a SiNC parent (PL peak = 886 nm, QY = 44%). (e) Bandgap deduced from the PL peak plotted as a function of SiNC diameter determined by TEM for a range of SiNC fractions, where the solid curve is the power law fit detailed in the text. The solid red square is from the computation model detailed in the text, and the gray markers are the recent experimental results of Yu et al.³ The solid curve is used to generate the diameters indicated on the top scale of panels (b) and (c). The excitation wavelength used for all optical measurements was 375 nm.

around 1.02 (parent PL peak ≥900 nm), where values <1.01 can be considered monodisperse. Such fractions can exhibit spontaneous formation of SiNC superlattice as Langmuir-Blodgett films (Figure 3d).

The results are summarized as a plot of E_g versus size (2R) in Figure 3e. For comparison, we include the recent results of Yu et al. for monodisperse suspensions synthesized using a nonplasma approach,3 where the solid curve is a fit to the expression $E = E_0 + A/(2R)^{\alpha}$, with $E_0 = 1.12 \text{ eV}$, A = 3.24, and a = 1.5. The data are also in qualitative agreement with the model introduced later in this contribution (red square). Perhaps the most striking feature is the implication for tunable SiNC emission. From the curve in Figure 3e, bandgaps corresponding to blue (450 nm) and green (500 nm) PL correspond to SiNC diameters of 1.6 and 1.8 nm, respectively, which is comparable to the size of the ligands commonly used to passivate these structures. Because of the strong impact of surface effects at these length scales, and the associated loss of PL QY, efficient blue/green core emission from SiNCs could thus be intrinsically difficult—if not impossible—to achieve, creating the need for surface-based approaches using chargetransfer ligands.

Analytical Ultracentrifugation. For an independent measure of SiNC size and dispersion state, we augment DGU with analytical ultracentrifugation (AUC). Primarily a tool of biochemistry, 67-69 AUC has recently emerged as a potentially powerful technique for characterizing nanoparticles. 70-72 In this approach, the absorption of an initially uniform suspension is optically monitored, while the colloid is centrifugally driven toward the bottom of the cell. The quantity

ACS Nano www.acsnano.org

of interest is the sedimentation coefficient (s) defined as the ratio of the sedimentation velocity to the applied acceleration: a characteristic time scale measured in Svedbergs (1 S = 10^{-13} s). AUC measurements were performed on both the parent (860 nm PL peak, 57% QY) and the color-coded fractions indicated in Figure 4. Note that the fraction with a PL peak at

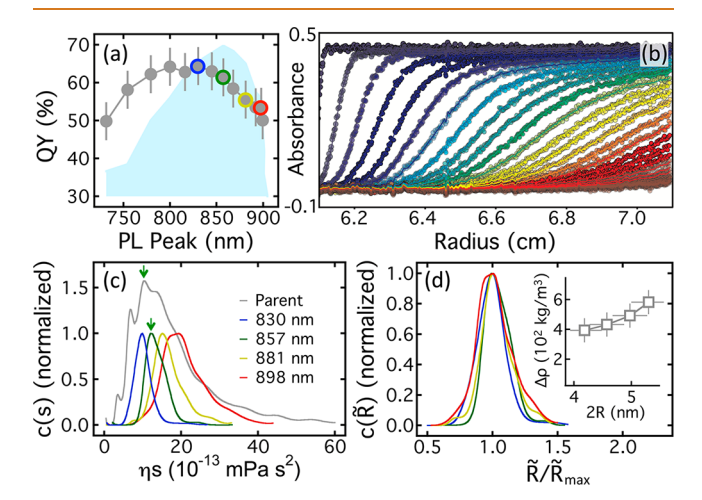


Figure 4. (a) QY versus PL peak for the DGU fractions prepared for AUC, where the shaded region indicates the absorption of each fraction (arbitrary scale/units). (b) Sedimentation profiles of absorbance versus centrifugal radius with the corresponding fit at varied times for the fraction indicated with yellow in panel (a). (c) Distribution of sedimentation coefficient for the parent suspension (gray) and each of the four fractions color coded in panel (a), where the green arrows indicate the common most probable size. (d) Hydrodynamic size distributions for each of the four fractions based on the data in panel (c), where the inset shows the effective $\Delta \rho$ as a function of TEM core size. Spectra in (c) and (d) have been normalized for ease of viewing.

850 nm (green marker) has the highest mass concentration based on optical absorption (shaded area, Figure 4a). A typical sedimentation profile is shown in Figure 4b. From a fit to the Lamm equation (solid curves, Figure 4b),68 we get the distribution of sedimentation coefficients, c(s), where

$$s = V \Delta \rho / (6\pi \eta f \tilde{R}) \tag{1}$$

Here, $V = V_C + V_L$ is the total volume of the SiNC core and ligand shell, where

$$\Delta \rho = (V_C \rho_C + V_L \rho_L) / (V_C + V_L) - \rho_S \tag{2}$$

and the subscripts C, L, and S in eq 2 denote "core", "ligand", and "solvent", respectively.⁶⁸ The parameter f = 1.24 is determined from the sedimentation fit, η is the solvent viscosity, and \tilde{R} is the hydrodynamic particle radius.⁶⁸

Figure 4c shows c(s) for the parent and fractions. Solvent viscosity varies (mesitylene for the parent and toluene for the fractions), so we use ηs on the horizontal scale. The green arrows indicate the most common hydrodynamic size, which also corresponds to the green marker in Figure 4a. Focusing on the fractions, we seek to convert the horizontal scale to hydrodynamic radius. The densities of mesitylene, toluene, mxylene, and 1-dodecene (864, 866.8, 860, and 758.4 kg/m³, respectively) are all close, implying that the shift in Figure 4c (green arrows) reflects a residual chloroform shell from DGU. Using

$$\tilde{R} = [9\eta fs/(2\Delta\rho)]^{1/2} \tag{3}$$

we define $\Delta \rho = \phi_C \rho_C + (1 - \phi_C) \rho_{L'} - \rho_S$, where $\rho_{L'}$ is the effective density of a solvent/ligand shell of thickness L (set to the contour length of 1-dodecene, 1.66 nm) and ϕ_C is the volume fraction of the silicon core. Our approach is to adjust $\Delta \rho$ as a free parameter to achieve $\tilde{R} = R + L$. Figure 4d shows the normalized $c(\tilde{R}/\tilde{R}_{max})$, where \tilde{R}_{max} is the most probable hydrodynamic radius based on the peaks in Figure 4c. The inset to Figure 4d shows $\Delta \rho$ versus TEM core diameter. Defining $\rho_L' = \phi_L \rho_L + (1 - \phi_L) \rho_{Ch}$, with ρ_L (758.4 kg/m³) and ρ_{Ch} (1489.2 kg/m³) denoting the densities of 1-dodecene and chloroform, respectively, these $\Delta \rho$ values are consistent with chloroform volume fractions of 0.38, 0.4, 0.46, and 0.48 (from smallest to largest) for the four fractions represented in Figure 4c,d.

The widths of the distributions in Figure 4d offer potential insight into SiNC dispersion state. The largest fraction (898 nm PL peak, red curves Figure 4) has a full-width-at-halfmaxium that is 22% higher than the other three, which we interpret as the emergence of small SiNC aggregates or clusters. We note that the same wavelength (900 nm) also corresponds to the emergence of an asymmetric PL line shape in the fractions (Figure 2a). The drop in QY indicated for the other fractions, however, correlates with increasing SiNC diameter, which further suggests that the QY maximum in the vicinity of 850 nm-both in the parents and in the fractions-is intrinsic to SiNCs and not a reflection of poor or incomplete passivation. From the data in Figure 2e, 850 nm PL corresponds to SiNC diameters of 4-5 nm, which is comparable to the exciton Bohr radius of silicon.

Early-Time Photoluminescence. Our last characterization approach focuses on the fast (ns) PL relaxation of the pristine SiNC fractions. The slow (μs) decay time of the size-separated samples follows the same qualitative trends as the parent suspensions (Figure 2e), although with longer lifetimes commensurate with higher QY (Figure S5). Here, we use a 35 fs pulsed laser to track PL emission as a function of wavelength and time over a 45 ns window for a range of SiNC core sizes. The excitation wavelength (400 nm) is close to the value of 375 nm used for all PL characterization in the preceding discussion, where both laser lines are well into the region of strong $\Gamma\Gamma$ absorption (Figure 2b). Details can be found in the Materials and Methods section. The results are presented in Figure 5. Representative time-dependent spectra corresponding to three different SiNC core diameters are shown in Figure 5a-c, as indicated by corresponding colors in a plot of QY versus PL peak wavelength (Figure 5d). The overlays show the PL spectra at t = 0.

There are three broad features in Figure 5a-c. The brightest and earliest is near 460 nm and decays quite quickly (\sim 100 ps) into a longer-lived shoulder near 500 nm (lifetime ≤ 1 ns). Note that the high-energy feature is truncated by the long-pass filter used to remove excitation from the PL signal. The earliest stages of the slow red PL decay are evident in Figure 5a,b, being off-scale in the NIR in Figure 5c. This last peak redshifts into the slow (μ s) decay (what we refer to as "PL peak" in this paper) over a time scale of several nanoseconds. 73 We interpret the multimodal fast PL decay as direct $(\Gamma\Gamma)$ radiative recombination. Using the language of Lee *et al.*, ¹² interfacial scattering leads to ΓX intervalley coupling and an increase in quasi-direct (zero-phonon) recombination. This mixing increases exponentially for smaller nanocrystals, but persists

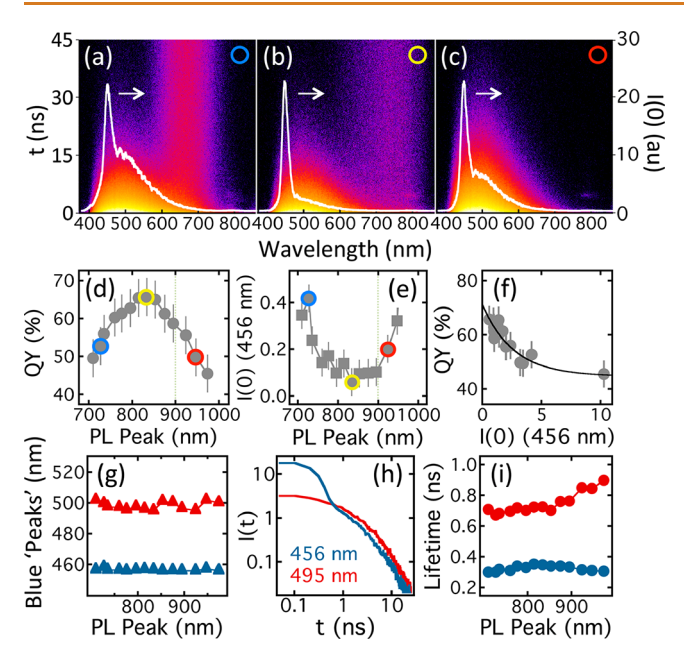


Figure 5. (a–c) Fast spectral PL decay (400 nm excitation) for the fractions indicated by colored circles in panel (d) viewed in the plane of emission wavelength and time (log intensity color scale). The white overlay shows the initial spectrum at t=0 (right scale), where the data are sector averaged over a ± 1.5 ns window around the initial peak to reduce noise. (d) QY versus PL peak for the fractions studied. (e) Initial (t=0) PL peak intensity (measured at 456 nm) versus PL peak for all of the fractions. (f) QY versus initial (t=0) PL peak intensity measured at 456 nm where the curve is an exponential decay with a large baseline. (g) Blue spectral features of interest versus PL peak and (h) corresponding fast PL decay for the data in panel (b). (i) Decay times (left scale) versus steady-state PL peak for the two spectral projections indicated on the right axis.

up to sizes near the Bohr radius. 12 Here, the physical picture is one of hot electrons recombining through the $\Gamma\Gamma$ channel, with the associated fast kinetics and high-energy emission. Because the SiNCs have been shielded from ambient conditions throughout processing, surface effects associated with exposure of the colloid to ambient oxygen can be ruled out.

Using the t=0 intensity of the "peak" near 460 nm as a measure of the strength of the $\Gamma\Gamma$ channel, Figure 5e shows the variation with PL peak for the fractions studied. To account for concentration, the intensity is normalized by the total

absorption of each fraction measured in an integrating sphere. A comparison of Figures 5d,e demonstrates that QY anticorrelates with the strength of the fast channel, with an extrapolation to zero abscissa (Figure 5f), suggesting a maximum achievable QY of 70% for the nanocrystals synthesized in this study. We note that upon opening the sample vial and exposing the fractions to ambient conditions, the intensity of the feature at 465 nm slowly decreases with time, commensurate with the associated drop in PL QY due to oxygen (Figure S6).

Reminiscent of the absorption in Figure 2b, the features of interest show little size dependence (Figure 5g). Time-dependent projections of the PL decay (Figure 5h) were fit to a stretched exponential decay with a stretching exponent of 0.5 to extract lifetimes, which likewise show only a weak dependence on size (Figure 5i). The stretching exponent was fixed to avoid having to use multiple free parameters to describe a limited window of data. Here, stretching again reflects a distribution of rates, but because these are zero-phonon transitions for hot electrons (the excitation energy is larger than 2× the gap for all but the smallest fractions), the distribution reflects different thermalization pathways from a range of initial states.

To explain the shape of Figure 5e, we turn to the AUC results presented previously, which suggest that a PL peak of around 900 nm (for comparable fractions obtained from a comparable parent) corresponds to the limit of SiNC dispersion and the appearance of aggregates in the fractions. From this, we conclude that the large value of I(0) at 456 nm for the two largest samples in Figure 5e is indicative of small SiNCs present in clusters, with this dispersion limit indicated as a vertical dashed line in Figure 5d,e. Focusing on the data to the left of this line, the intensity of the fast decay mode increases steeply with decreasing nanocrystal size, which is accompanied by a drop in QY.

For simplicity, we assume the PL originates from two different channels, $\Gamma\Gamma$ and $X\Gamma$ with associated rate constants $k_{\Gamma\Gamma}=k_{\Gamma\Gamma_R}+k_{\Gamma\Gamma_{NR}}$ and $k_{X\Gamma}=k_{X\Gamma_R}+k_{X\Gamma_{NR}}$, where the subscripts R and NR denote radiative and nonradiative, respectively. The corresponding lifetimes are $\tau_{\Gamma\Gamma}=1/k_{\Gamma\Gamma}$ (Figure 5i) and $\tau_{\Gamma\Gamma_R}=1/k_{\Gamma\Gamma_R}$ for the fast channel, with $\tau_{X\Gamma}=1/k_{X\Gamma}$ and $\tau_{X\Gamma_R}=1/k_{X\Gamma_{NR}}$ for the slow channel (Figure S5). We can assume narrow rate distributions without any loss of generality, with the time-dependent PL given by

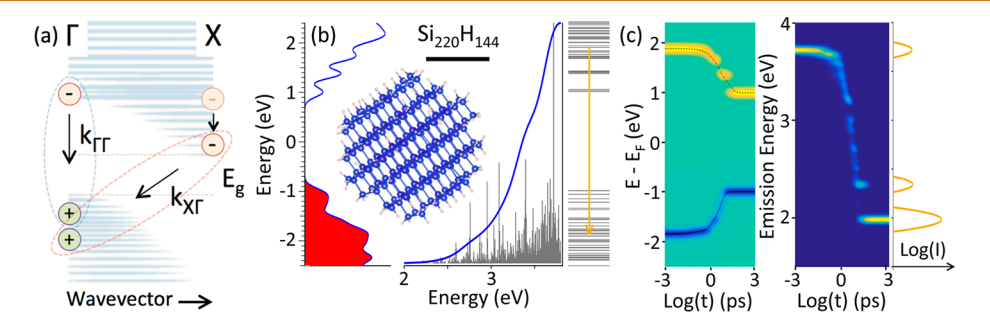


Figure 6. (a) Schematic in k-space of the two channels $\Gamma\Gamma$ and ΓX . (b) Computed DOS (left) and absorption spectrum (middle) for the simulated SiNC (1 nm scale bar). The corresponding energy levels are indicated on the right. (c) Simulated excited-state trajectories (left) for the electron (yellow) and hole (blue) and the corresponding fast PL decay (middle, with time-averaged PL peaks indicated at right) computed for the relaxation pathway depicted in yellow on the right side of panel (b).

$$I(t) = \left(\frac{\phi_{\Gamma\Gamma}}{\tau_{\Gamma\Gamma_{R}}}\right) \exp(-t/\tau_{\Gamma\Gamma}) + \left(\frac{\phi_{X\Gamma}}{\tau_{X\Gamma_{R}}}\right) \exp(-t/\tau_{X\Gamma})$$
(4)

Each term in eq 4 is weighted by the appropriate rate constant, $\phi_{\Gamma\Gamma}$ and $\phi_{X\Gamma}$ denote the fraction of emitters in each channel $(\phi_{X\Gamma} + \phi_{\Gamma\Gamma} = 1)$, and the corresponding QY is⁶¹

$$\Phi = \phi_{\Gamma\Gamma}(\tau_{\Gamma\Gamma}/\tau_{\Gamma\Gamma_R}) + \phi_{X\Gamma}(\tau_{X\Gamma}/\tau_{X\Gamma_R})$$
 (5)

The quantities I(0), $\tau_{\Gamma\Gamma}$, $\tau_{X\Gamma}$, and Φ are all measured. Focusing on the fraction indicated in yellow in Figure 5b $[\Phi=65\%,\tau_{X\Gamma}=195~\mu s,\tau_{\Gamma\Gamma}\leq 1~\rm ns,$ and $I_{\Gamma\Gamma}(0)/I_{X\Gamma}(0)=110]$, eq 4 gives $I_{\Gamma\Gamma}(0)/I_{X\Gamma}(0)=(\phi_{\Gamma\Gamma}/\phi_{X\Gamma})(\tau_{X\Gamma_R}/\tau_{\Gamma_R})\approx 10^2$. With $\tau_{X\Gamma_R}$ on the order of hundreds of μs and $\tau_{\Gamma\Gamma_R}$ on the order of nanoseconds, we get $\phi_{\Gamma\Gamma}/\phi_{X\Gamma}\approx 10^{-3}$. Although the $\Gamma\Gamma$ channel dominates the PL decay at early time, it makes no measurable contribution to the QY. For nanocrystals in general, the energy landscape of carriers is strongly influenced by the nanocrystal surface, τ^{74} and we suggest that both the strengthening of the quasi-direct $\Gamma\Gamma$ channel and the drop in QY for smaller SiNCs (Figure 5e) are consequences of surface effects

Computational Modeling. The two radiative channels are represented schematically in Figure 6a. To gain physical insight into the fast multistep PL relaxation process, we consider a computational model of hot carrier relaxation applied to a SiNC of realistic size. Specifically, we consider a 2.1 nm diameter SiNC surface passivated with hydrogen (Si₂₂₀H₁₄₄), where the ground-state electronic structure is calculated with density functional theory (DFT) in the Vienna *ab initio* simulation package (VASP). Figure 6b shows the computed density-of-states (DOS), the computed absorption spectrum, and the corresponding energy levels, where the effective bandgap falls on the curve derived from the experiments (red marker, Figure 3e). Details can be found in the Supporting Information

We consider the specific relaxation pathway represented by the orange arrow. A description of hot carriers requires explicit treatment of the coupling between nuclear and electronic degrees of freedom. Here, such electron-phonon interactions are considered through the computation of "on-the-fly" nonadiabatic couplings from adiabatic molecular dynamics trajectories.⁷⁵ Redfield tensor components in the density matrix formalism are then obtained by numerically processing the autocorrelation function of these couplings. Details can be found in the Supporting Information. The left panel of Figure 6c shows the relaxation of charge carriers as a function of energy and time after an instantaneous photoexcitation at t = 0that generates a hot electron at LUMO+38 and a hot hole at HOMO-37. Yellow, blue, and green correspond to electron gain, hole gain, and no gain in population with respect to equilibrium, respectively, and the solid and dashed curves represent the expectation value of carrier energy. The right panel of Figure 6c shows the corresponding PL. Despite significant energy loss, both the electron and hole reach the frontier orbitals with limited recombination. Although the energy scales can be compared directly, the times scales are significantly different due to the simplified nature of electronphonon coupling. However, the simulations reproduce the physical trends suggested by the experiments. Hot carriers thermalize to the band edge through a broad distribution of possible states, which is accompanied by a weak component of fast ($\Gamma\Gamma$) PL. Once at the band edge, the carriers "wait" for the required conditions for the more dominant $X\Gamma$ recombination.

In a broader view, the fast PL is simply a weak radiative signature of much larger interfacial effects, which in turn have a detrimental effect on QY through their associated nonradiative channels. This is what underlies the trend shown in Figure 5f. That these surface effects persist up to the exciton Bohr radius (Figure 5e) is consistent with the anticipated interplay between quantum confinement and interfacial scattering, and the distinction between "quasi-direct" and "surface" becomes somewhat blurry. The magnitude of $\phi_{\Gamma\Gamma}/\phi_{Y\Gamma}$ suggested by the simulations (right side, Figure 6c) is \sim 1%. For a hot electron, the probability of thermalization to adjacent lower energy states is much higher than that of radiative recombination, so we expect this ratio to be small. However, this is still an order-of-magnitude larger than the experimental values (~0.1%), and other factors beyond size are potentially at play. In this regard, it is useful to look at similarly sized fractions derived from different sized parents, as detailed in the Supporting Information (Figure S5). Our data suggest that there is an optimum target SiNC size for achieving maximum QY. Although the same components (CHS, carrier gas, and injected hydrogen) are used for every parent, we cannot rule out the possibility that defects and/or impurities might also play a role in the fast emission. However, this question is beyond the scope of the present study.

CONCLUSIONS

In conclusion, we demonstrate the utility of the liquid precursor cyclohexasilane (Si₆H₁₂) for the plasma synthesis of colloidal SiNCs with pristine PL QYs approaching 70%. Liquid silane precursors offer clear safety advantages over silane gas as well as the potential for improved scalability and yield. By separating the nanocrystals into size-resolved fractions without exposing them to ambient oxygen, we reveal important intrinsic constraints on efficient PL from smaller SiNCs, with blue/green core emission corresponding to nanocrystal diameters that are likely too small to be viable as a freestanding colloid, although core/shell architectures may still hold particular promise here. In response to femtosecond pulsed excitation, time-resolved PL spectra of the pristine fractions reveal a quasi-direct radiative channel that anticorrelates with QY, which we suggest is a consequence of surface effects. In this view, the fast mode is simply a weak radiative indicator of the influence of the interface, which itself has a detrimental impact on the efficiency of the much more predominant indirect recombination. The multimodal nature of the fast PL is modeled using advanced computational methods applied to a 2 nm SiNC. Collectively, our results offer further insight into the photophysical constraints and limitations that underlie the PL from colloidal SiNCs as well as the nature of the interplay between the nanocrystal surface and efficient core emission. At very early times (≤ 1 ns), it is reasonable to assume that hot carriers with large energy separation are strongly influenced by the large lattice vibrations found at the nanocrystal surface. In a qualitative sense, this is the "surface scattering" that mixes quasi-direct $\Gamma\Gamma$ character into the conduction band states, and we suggest that the fast PL reported here is simply a very weak radiative signature of this mixing.

MATERIALS AND METHODS

CHS Synthesis. Details of the synthesis and purification of CHS are described elsewhere. Crude CHS was obtained from the reduction of [(Et₂NCH₂CH₂)₂NEt·H₂SiCl]₂[Si₆Cl₁₄] with LiAlH₄ in diethyl ether. The resulting reaction mixture was filtered, and the filtrate was concentrated under reduced pressure. CHS was extracted from the filtrate using *n*-pentane, and the dilute extract was washed with 9 N H₂SO₄ under rigorously controlled conditions. The organic layer was dried over Na₂SO₄ prior to isolation of purified CHS by fractional vacuum distillation.

Nanocrystal Synthesis. Silicon nanocrystals were prepared via the nonthermal plasma synthesis method pioneered by Mangolini et $al._{1}^{50}$ with side port injection of hydrogen described by Jurbergs ei $al._{1}^{51}$ and Anthony et $al._{1}^{47}$ A bubbler containing CHS was used for precursor delivery. For the bulk of the SiNCs characterized in this study, the downstream end of the reactor vessel was set to 127 Pa and the CHS was kept at 0.3 sccm. The carrier gas consisted of 95% argon and 5% hydrogen (research grade) and was varied from 20 to 200 sccm as a way to tune nanocrystal size, while the hydrogen injected in the side port was varied from 0 to 100 sccm. Optimal QY (around 60% near 850 nm peak emission) was typically achieved using approximately 45 sccm of carrier gas and 100 sccm of injected hydrogen. For surface passivation, samples were collected on stainless steel mesh and transferred to microwave reaction vials containing mesitylene and 1-dodecene (at a 5:1 ratio) and heated to 185 °C. All steps were carried out in a nitrogen environment, and all organic solvents used were purchased as anhydrous or were subjected to a freeze-pump-thaw protocol. While CHS has been previously used to synthesize silicon nanorods and nanoparticles, 59,76 among several other things, it has never been used to synthesize SiNCs that exhibit bandgap emission.

Ultracentrifugation. DGU was performed in a Beckman Coulter Optima L-80 XP ultracentrifuge using m-xylene/chloroform gradients in custom centrifuge tubes as detailed in the Supporting Information. AUC was conducted in a Beckman-Coulter XL-I analytical ultracentrifuge with a Ti-50 rotor using 12 mm optical path length aluminum centerpiece cells with sapphire windows. Measurements were performed at 20.0 °C and a rotation rate of 2932 rad/s (28 kRPM), starting rotation after a minimum of 1.5 h of temperature equilibration. Radial absorbance scans were measured at 320 nm. The density and viscosity of neat mesitylene and toluene were independently determined with an Anton-Parr DMA 5000 - LOVIS M densitometer-viscometer. For AUC, DGU fractions were exchanged from the mixed solvent in which they were recovered into neat toluene via precipitation with ethanol/centrifugation and repeatedly diluted with toluene and dried under an argon gas flow before final dilution with toluene. Radial absorbance profiles as a function of time were analyzed using the numerical fitting software SEDFIT version 15.01b. 67,68,71 Sedimentation was modeled using the c(s) with best-fit values utilized for the meniscus position and the parameter f.

Transmission Electron Microscopy. For TEM, SiNC samples were cast on DEG (diethylene glycol) in a Teflon Langmuir—Blodgett trough and dried under a glass coverslip. The SiNC monolayer was collected on a graphene-coated TEM grid (PELCO single-layer graphene on lacey carbon with 300 mesh copper grids), and the grid was vertically introduced into DI water for 1 min and then into chloroform for 30 s to remove DEG and mesitylene before being dried under vacuum for 48 h. HRTEM images were collected with a JEOL JEM2100 LaB6 transmission electron microscope equipped with a Gatan Orius SC1000 CCD camera. ImageJ was used for sizing "by-hand" using more than 100 SiNCs per sample.

Photoluminescence Spectroscopy. PL QY was measured with an integrating sphere fiber-coupled through a bifurcated UV/vis and vis/NIR fiber to Ocean Optics QE65000 and NIRQ512 spectrometers (350–1700 nm detection), with 375 nm CW laser excitation at 4.2 mW. Spectral shape was instrument-corrected using the blackbody emission from a tungsten filament as a reference, and the QY was calibrated against multiple samples representing five different

standards with emission spanning the visible spectrum. QY was measured at SiNC concentrations of 1 mg/mL or less and was confirmed to be independent of concentration up to 2 mg/mL. For the slow PL lifetime, modulated pulsed excitation was delivered through a notch filter with a fiber-coupled pulsed UV laser (Advanced Laser Diode Systems, PiL037, 375 nm, 30 ps pulse width, 140 mW peak power, 1 kHz modulation) fiber coupled to a photomultiplier tube. A 10× objective was used in EPI illumination. For fast PL relaxation measurements, as-received pristine fractions were excited in a front-face configuration using the 400 nm, frequency-doubled output of a 35 fs, Ti:sapphire laser operating at a frequency of 2 kHz. Emission from the NCs was detected through two 435 nm long-pass filters using a single-photon sensitive streak camera. Measurements were performed on dilute colloidal SiNC suspensions sealed in glass vials to protect from O₂ exposure.

Nanocrystal Characterization. Raman spectroscopy was performed using a HORIBA Jobin Yvon LabRAM ARAMIS confocal imaging system using 532 nm excitation and a 50× objective. Diffuse reflectance FTIR spectra were collected with a Bruker Alpha FTIR spectrometer. XRD data was collected from dried samples using a Bruker D8 Discover X-ray diffractometer, with the substrate background measured and removed. FTIR spectra were collected using a Thermo Scientific Nicolet 8700 with attenuated total reflectance (ATR) capabilities (NDSU) and a Bruker Alpha II with diffuse-reflectance capabilities mounted inside a glovebox (UMN). TGA was performed using a TA TGA Q500. XPS data was collected using a Thermo Scientific K-Alpha XPS system.

Certain equipment, instruments, or materials are identified in this paper in order to adequately specify the experimental details. Such identification does not imply recommendation by the National Institute of Standards and Technology (NIST) nor does it imply the materials are necessarily the best available for the purpose.

ASSOCIATED CONTENT

Supporting Information

The Supporting Information is available free of charge at https://pubs.acs.org/doi/10.1021/acsnano.9b09614.

Description of the DGU process, TEM images and size distributions of the parents and fractions, additional FTIR spectra, TGA analysis, XPS data, slow PL lifetime and QY data for parents and fractions, oxygen exposure experiments, a table of the photophysical attributes of high-QY fractions, and a description of the computational model (PDF)

AUTHOR INFORMATION

Corresponding Authors

Todd A. Pringle — Materials and Nanotechnology Program, North Dakota State University, Fargo, North Dakota 58108, United States; Email: todd.pringle@twilight-labs.com

Erik K. Hobbie — Materials and Nanotechnology Program,
Department of Physics, and Department of Coatings and
Polymeric Materials, North Dakota State University, Fargo,
North Dakota 58108, United States; orcid.org/0000-0001-6158-8977; Email: erik.hobbie@ndsu.edu

Authors

Katharine I. Hunter — Department of Mechanical Engineering, University of Minnesota, Minneapolis, Minnesota 55455, United States; Occid.org/0000-0001-8639-5012

Alexandra Brumberg — Department of Chemistry, Northwestern University, Evanston, Illinois 60208, United States;
orcid.org/0000-0003-2512-4686

Kenneth J. Anderson – Department of Chemistry & Biochemistry, North Dakota State University, Fargo, North Dakota 58108, United States

- Jeffrey A. Fagan National Institute of Standards and Technology, Gaithersburg, Maryland 20899, United States; orcid.org/0000-0003-1483-5554
- Salim A. Thomas Materials and Nanotechnology Program, North Dakota State University, Fargo, North Dakota 58108, United States
- Reed J. Petersen Department of Physics, North Dakota State University, Fargo, North Dakota 58108, United States
- Mahmud Sefannaser Department of Physics, North Dakota State University, Fargo, North Dakota 58108, United States
- Yulun Han Department of Chemistry & Biochemistry, North Dakota State University, Fargo, North Dakota 58108, United States
- Samuel L. Brown Materials and Nanotechnology Program, North Dakota State University, Fargo, North Dakota 58108, United States
- Dmitri S. Kilin Department of Chemistry & Biochemistry, North Dakota State University, Fargo, North Dakota 58108, United States
- Richard D. Schaller Department of Chemistry, Northwestern University, Evanston, Illinois 60208, United States; Center for Nanoscale Materials, Argonne National Laboratory, Argonne, Illinois 60439, United States
- **Uwe R. Kortshagen** − Department of Mechanical Engineering, University of Minnesota, Minneapolis, Minnesota 55455, United States; orcid.org/0000-0001-5944-3656
- Philip Raymond Boudjouk Department of Chemistry & Biochemistry, North Dakota State University, Fargo, North Dakota 58108, United States; orcid.org/0000-0001-7866-5000

Complete contact information is available at: https://pubs.acs.org/10.1021/acsnano.9b09614

Notes

The authors declare no competing financial interest.

ACKNOWLEDGMENTS

E.K.H. acknowledges support from the National Science Foundation through CBET-1603445. K.I.H. acknowledges support from the National Science Foundation Graduate Research Fellowship Program under grant number 00039202. A.B. acknowledges support though the National Science Foundation Graduate Research Fellowship Program under DGE-1324585. D.K. acknowledges support from the DOE through DE-AC02-05CH11231 and the NSF through CHE-1800476 and OIA-1355466. The authors also acknowledge support of National Institute of Standards and Technology (NIST) internal funding.

REFERENCES

- (1) Mazzaro, R.; Romano, F.; Ceroni, P. Long-Lived Luminescence of Silicon Nanocrystals: From Principles to Applications. *Phys. Chem. Chem. Phys.* **2017**, *19*, 26507–26526.
- (2) Meinardi, F.; Ehrenberg, S.; Dhamo, L.; Carulli, F.; Mauri, M.; Bruni, F.; Simonutti, R.; Kortshagen, U.; Brovelli, S. Highly Efficient Luminescent Solar Concentrators Based on Earth-Abundant Indirect-Bandgap Silicon Quantum Dots. *Nat. Photonics* **2017**, *11*, 177–185.
- (3) Yu, Y.; Fan, G.; Fermi, A.; Mazzaro, R.; Morandi, V.; Ceroni, P.; Smilgies, D.-M.; Korgel, B. A. Size-Dependent Photoluminescence Efficiency of Silicon Nanocrystal Quantum Dots. *J. Phys. Chem. C* **2017**, *121*, 23240–23248.
- (4) Hannah, D. C.; Yang, J.; Podsiadlo, P.; Chan, M. K.; Demortiere, A.; Gosztola, D. J.; Prakapenka, V. B.; Schatz, G. C.; Kortshagen, U.;

- Schaller, R. D. On the Origin of Photoluminescence in Silicon Nanocrystals: Pressure-Dependent Structural and Optical Studies. *Nano Lett.* **2012**, *12*, 4200–4205.
- (5) Miller, J. B.; Van Sickle, A. R.; Anthony, R. J.; Kroll, D. M.; Kortshagen, U. R.; Hobbie, E. K. Ensemble Brightening and Enhanced Quantum Yield in Size-Purified Silicon Nanocrystals. *ACS Nano* **2012**, *6*, 7389–7396.
- (6) Mastronardi, M. L.; Maier-Flaig, F.; Faulkner, D.; Henderson, E. J.; Kübel, C.; Lemmer, U.; Ozin, G. A. Size-Dependent Absolute Quantum Yields for Size-Separated Colloidally-Stable Silicon Nanocrystals. *Nano Lett.* **2012**, *12*, 337–342.
- (7) Delerue, C.; Allan, G.; Reynaud, C.; Guillois, O.; Ledoux, G.; Huisken, F. Multiexponential Photoluminescence Decay in Indirect-Gap Semiconductor Nanocrystals. *Phys. Rev. B: Condens. Matter Mater. Phys.* **2006**, 73, 235318.
- (8) Brown, S. L.; Krishnan, R.; Elbaradei, A.; Sivaguru, J.; Sibi, M. P.; Hobbie, E. K. Origin of Stretched-Exponential Photoluminescence Relaxation in Size-Separated Silicon Nanocrystals. *AIP Adv.* **2017**, *7*, 055314.
- (9) Greben, M.; Khoroshyy, P.; Liu, X.; Pi, X.; Valenta, J. Fully Radiative Relaxation of Silicon Nanocrystals in Colloidal Ensemble Revealed by Advanced Treatment of Decay Kinetics. *J. Appl. Phys.* **2017**, *122*, 034304.
- (10) Sangghaleh, F.; Bruhn, B.; Schmidt, T.; Linnros, J. Exciton Lifetime Measurements on Single Silicon Quantum Dots. *Nanotechnology* **2013**, *24*, 225204.
- (11) Takagahara, T.; Takeda, K. Theory of the Quantum Confinement Effect on Excitons in Quantum Dots of Indirect-Gap Materials. *Phys. Rev. B: Condens. Matter Mater. Phys.* **1992**, 46, 15578–15581.
- (12) Lee, B. J.; Luo, J.-W.; Neale, N. R.; Beard, M. C.; Hiller, D.; Zacharias, M.; Stradins, P.; Zunger, A. Quasi-Direct Optical Transitions in Silicon Nanocrystals with Intensity Exceeding the Bulk. *Nano Lett.* **2016**, *16*, 1583–1589.
- (13) Sangghaleh, F.; Sychugov, I.; Yang, Z.; Veinot, J. G. C.; Linnros, J. Near-Unity Internal Quantum Efficiency of Luminescent Silicon Nanocrystals with Ligand Passivation. *ACS Nano* **2015**, *9*, 7097–7104
- (14) Wen, X.; Zhang, P.; Smith, T. A.; Anthony, R. J.; Kortshagen, U. R.; Yu, P.; Feng, Y.; Shrestha, S.; Coniber, G.; Huang, S. Tunability Limit of Photoluminescence in Colloidal Silicon Nanocrystals. *Sci. Rep.* **2015**, *5*, 12469.
- (15) Sagar, D. M.; Atkin, J. M.; Palomaki, P. K. B.; Neale, N. R.; Blackburn, J. L.; Johnson, J. C.; Nozik, A. J.; Raschke, M. B.; Beard, M. C. Quantum Confined Electron-Phonon Interaction in Silicon Nanocrystals. *Nano Lett.* **2015**, *15*, 1511–1516.
- (16) Sychugov, I.; Fucikova, A.; Pevere, F.; Yang, Z.; Veinot, J. G. C.; Linnros, J. Ultranarrow Luminescence Linewidth of Silicon Nanocrystals and Influence of Matrix. ACS Photonics 2014, 1, 998–1005.
- (17) Miller, J. B.; Dandu, N.; Velizhanin, K. A.; Anthony, R. J.; Kortshagen, U. R.; Kroll, D. M.; Kilina, S.; Hobbie, E. K. Enhanced Luminescent Stability through Particle Interactions in Silicon Nanocrystal Aggregates. ACS Nano 2015, 9, 9772–9782.
- (18) Brown, S. L.; Vogel, D. J.; Miller, J. B.; Inerbaev, T. M.; Anthony, R. J.; Kortshagen, U. R.; Kilin, D. S.; Hobbie, E. K. Enhancing Silicon Nanocrystal Photoluminescence through Temperature and Microstructure. *J. Phys. Chem. C* **2016**, *120*, 18909–18916.
- (19) Van Sickle, A. R.; Miller, J. B.; Moore, C.; Anthony, R. J.; Kortshagen, U. R.; Hobbie, E. K. Temperature Dependent Photoluminescence of Size-Purified Silicon Nanocrystals. *ACS Appl. Mater. Interfaces* **2013**, *5*, 4233–4238.
- (20) Marinins, A.; Zandi Shafagh, R.; van der Wijngaart, W.; Haraldsson, T.; Linnros, J.; Veinot, J. G. C.; Popov, S.; Sychugov, I. Light-Converting Polymer/Si Nanocrystal Composites with Stable 60–70% Quantum Efficiency and Their Glass Laminates. *ACS Appl. Mater. Interfaces* **2017**, *9*, 30267–30272.
- (21) Ondič, L.; Kusová, K.; Ziegler, M.; Fekete, L.; Gärtnerová, V.; Cháb, V.; Holý, V.; Cibulka, O.; Herynková, K.; Gallart, M.; Gilliot, P.; Hönerlage, B.; Pelant, I. A Complex Study of the Fast Blue

- Luminescence of Oxidized Silicon Nanocrystals: The Role of the Core. *Nanoscale* **2014**, *6*, 3837–3845.
- (22) Hannah, D. C.; Yang, J.; Kramer, N. J.; Schatz, G. C.; Kortshagen, U. R.; Schaller, R. D. Ultrafast Photoluminescence in Quantum-Confined Silicon Nanocrystals Arises from an Amorphous Surface Layer. *ACS Photonics* **2014**, *1*, 960–967.
- (23) Kůsová, K.; Ondič, L.; Pelant, I. Comment on "Ultrafast Photoluminescence in Quantum-Confined Silicon Nanocrystals Arises from an Amorphous Surface Layer. ACS Photonics 2015, 2, 454–455.
- (24) Yang, Z.; De los Reyes, G. B.; Titova, L. V.; Sychugov, I.; Dasog, M.; Linnros, J.; Hegmann, F. A.; Veinot, J. G. C. Evolution of the Ultrafast Photoluminescence of Colloidal Silicon Nanocrystals with Changing Surface Chemistry. *ACS Photonics* **2015**, *2*, 595–605.
- (25) Brown, S. L.; Miller, J. B.; Anthony, R. J.; Kortshagen, U. R.; Kryjevski, A.; Hobbie, E. K. Abrupt Size Partitioning of Multimodal Photoluminescence Relaxation in Monodisperse Silicon Nanocrystals. *ACS Nano* **2017**, *11*, 1597–1603.
- (26) de Boer, W. D. A. M. D.; Timmerman, K.; Dohnalová, I. N.; Yassievich, H.; Zhang, W.; Buma, J.; Gregorkiewicz, T. Red Spectral Shift and Enhanced Quantum Efficiency in Phonon-Free Photoluminescence from Silicon Nanocrystals. *Nat. Nanotechnol.* **2010**, 5, 878—884
- (27) Sychugov, I.; Valenta, J.; Mitsuishi, K.; Fujii, M.; Linnros, J. Photoluminescence Measurements of Zero-Phonon Optical Transitions in Silicon Nanocrystals. *Phys. Rev. B: Condens. Matter Mater. Phys.* **2011**, 84, 125326.
- (28) Dohnalová, K.; Poddubny, A. N.; Prokofiev, A. A.; de Boer, W. D. A. M.; Umesh, C. P.; Paulusse, J. M. J.; Zuilhof, H.; Gregorkiewicz, T. Surface Brightens Up Si Quantum Dots: Direct Bandgap-Like Size-Tunable Emission. *Light: Sci. Appl.* **2013**, *2*, No. e47.
- (29) Kim, S.; Shin, D. H.; Choi, S.-H. Ultrafast Photoluminescence from Freestanding Si Nanocrystals. *Appl. Phys. Lett.* **2012**, *100*, 253103.
- (30) Dohnalova, K.; Gregorkiewicz, T.; Kusova, K. Silicon Quantum Dots: Surface Matters. J. Phys.: Condens. Matter 2014, 26, 173201.
- (31) Poddubny, A. N.; Dohnalová, K. Direct Band Gap Silicon Quantum Dots Achieved via Electronegative Capping. Phys. Rev. B: Condens. Matter Mater. Phys. 2014, 90, 245439.
- (32) Prokofiev, A. A.; Moskalenko, A. S.; Yassievich, I. N.; de Boer, W. D. A. M.; Timmerman, D.; Zhang, H.; Buma, W. J.; Gregorkiewicz, T. Direct Bandgap Optical Transitions in Si Nanocrystals. *JETP Lett.* **2010**, *90*, 758–762.
- (33) Kocevski, V.; Eriksson, O.; Rusz, J. Transition between Direct and Indirect Band Gap in Silicon Nanocrystals. *Phys. Rev. B: Condens. Matter Mater. Phys.* **2013**, 87, 245401.
- (34) Kůsová, K. Silicon Nanocrystals: From Indirect to Direct Bandgap. *Phys. Status Solidi A* **2018**, 215, 1700718.
- (35) Hapala, P.; Kůsová, K.; Pelant, I.; Jelínek, P. Theoretical Analysis of Electronic Band Structure of 2- to 3-Nm Si Nanocrystals. *Phys. Rev. B: Condens. Matter Mater. Phys.* **2013**, *87*, 195420.
- (36) Dasog, M.; De los Reyes, G. B.; Titova, L. V.; Hegmann, F. A.; Veinot, J. G. C. Size *versus* Surface: Tuning the Photoluminescence of Freestanding Silicon Nanocrystals across the Visible Spectrum *via* Surface Groups. *ACS Nano* **2014**, *8*, 9636–9648.
- (37) Sinelnikov, R.; Dasog, M.; Beamish, J.; Meldrum, A.; Veinot, J. G. C. Revisiting an Ongoing Debate: What Role Do Surface Groups Play in Silicon Nanocrystal Photoluminescence? *ACS Photonics* **2017**, *4*, 1920–1929.
- (38) Li, Q.; Luo, T.-Y.; Zhou, M.; Abroshan, H.; Huang, J.; Kim, H. J.; Rosi, N. L.; Shao, S.; Jin, R. Silicon Nanoparticles with Surface Nitrogen: 90% Quantum Yield with Narrow Luminescence Bandwidth and the Ligand Structure Based Energy Law. *ACS Nano* **2016**, *10*, 8385–8393.
- (39) So, W. Y.; Li, Q.; Legaspi, C. M.; Redler, B.; Koe, K. M.; Jin, R.; Peteanu, L. A. Mechanism of Ligand-Controlled Emission in Silicon Nanoparticles. *ACS Nano* **2018**, *12*, 7232–7238.
- (40) Rosso-Vasic, M.; Spruijt, E.; Popovic, Z.; Overgaag, K.; van Lagen, B.; Grandidier, B.; Vanmaekelbergh, D.; Dominguez-Gutierrez,

- D.; De Cola, L.; Zuilhof, H. Amine- Terminated Silicon Nanoparticles: Synthesis, Optical Properties and Their Use in Bioimaging. *J. Mater. Chem.* **2009**, *19*, 5926–5933.
- (41) Kůsová, K.; Cibulka, O.; Dohnalová, K.; Pelant, I.; Valenta, J.; Fučiková, A.; Zidek, K.; Lang, J.; Englich, J.; Matéjka, P.; Štěpánek, P.; Bakardjieva, S. Brightly Luminescent Organically Capped Silicon Nanocrystals Fabricated at Room Temperature and Atmospheric Pressure. ACS Nano 2010, 4, 4495–4504.
- (42) Hessel, C. M.; Reid, D.; Panthani, M. G.; Rasch, M. R.; Goodfellow, B. W.; Wei, J.; Fujii, H.; Akhavan, V.; Korgel, B. A. Synthesis of Ligand-Stabilized Silicon Nanocrystals with Size-Dependent Photoluminescence Spanning Visible to Near-Infrared Wavelengths. *Chem. Mater.* **2012**, *24*, 393–401.
- (43) Islam, M. A.; Mobarok, M. H.; Sinelnikov, R.; Purkait, T. K.; Veinot, J. G. C. Phosphorus Pentachloride Initiated Functionalization of Silicon Nanocrystals. *Langmuir* **2017**, *33*, 8766–8773.
- (44) Mobarok, M. H.; Purkait, T. K.; Islam, M. A.; Miskolzie, M.; Veinot, J. G. C. Instantaneous Functionalization of Chemically Etched Silicon Nanocrystal Surfaces. *Angew. Chem., Int. Ed.* **2017**, *56*, 6073–6077.
- (45) Sugimoto, H.; Yamamura, M.; Fujii, R.; Fujii, M. Donor-Acceptor Pair Recombination in Size-Purified Silicon Quantum Dots. *Nano Lett.* **2018**, *18*, 7282–7288.
- (46) Kortshagen, U. R.; Sankaran, R. M.; Pereira, R. N.; Girshick, S. L.; Wu, J. J.; Aydil, E. S. Nonthermal Plasma Synthesis of Nanocrystals: Fundamental Principles, Materials, and Applications. *Chem. Rev.* **2016**, *116*, 11061–11127.
- (47) Anthony, R. J.; Rowe, D. J.; Stein, M.; Yang, J.; Kortshagen, U. Routes to Achieving High Quantum Yield Luminescence from Gas-Phase-Produced Silicon Nanocrystals. *Adv. Funct. Mater.* **2011**, *21*, 4042–4046.
- (48) Gresback, R.; Nozaki, T.; Okazaki, K. Synthesis and Oxidation of Luminescent Silicon Nanocrystals from Silicon Tetrachloride by Very High Frequency Nonthermal Plasma. *Nanotechnology* **2011**, *22*, 305605.
- (49) Yasar-Inceoglu, O.; Lopez, T.; Farshihagro, E.; Mangolini, L. Silicon Nanocrystal Production through Non-thermal Plasma Synthesis: A Comparative Study between Silicon Tetrachloride and Silane Precursors. *Nanotechnology* **2012**, *23*, 255604.
- (50) Mangolini, L.; Thimsen, L.; Kortshagen, U. High-Yield Plasma Synthesis of Luminescent Silicon Nanocrystals. *Nano Lett.* **2005**, *5*, 655–659.
- (51) Jurbergs, D.; Rogojina, E.; Mangolini, L.; Kortshagen, U. Silicon Nanocrystals with Ensemble Quantum Yields Exceeding 60%. *Appl. Phys. Lett.* **2006**, *88*, 233116.
- (52) Mangolini, L. Synthesis, Properties, and Applications of Silicon Nanocrystals. J. Vac. Sci. Technol., B: Nanotechnol. Microelectron.: Mater., Process., Meas., Phenom. 2013, 31, 020801.
- (53) Pi, X. D.; Gresback, R.; Liptak, R. W.; Campbell, S. A.; Kortshagen, U. Doping Efficiency, Dopant Location, and Oxidation of Si Nanocrystals. *Appl. Phys. Lett.* **2008**, 92, 123102.
- (54) Oliva-Chatelain, B. L.; Ticich, T. M.; Barron, A. R. Doping Silicon Nanocrystals and Quantum Dots. *Nanoscale* **2016**, *8*, 1733–1745.
- (55) Hunter, K. I.; Held, J. T.; Mkhoyan, K. A.; Kortshagen, U. R. Nonthermal Plasma Synthesis of Core/Shell Quantum Dots: Strained Ge/Si Nanocrystals. *ACS Appl. Mater. Interfaces* **2017**, *9*, 8263–8270.
- (56) Wheeler, L. M.; Anderson, N. C.; Palomaki, P. K. B.; Blackburn, J. L.; Johnson, J. C.; Neale, N. R. Silyl Radical Abstraction in the Functionalization of Plasma-Synthesized Silicon Nanocrystals. *Chem. Mater.* **2015**, *27*, 6869–6878.
- (57) Masuda, T.; Takagishi, H.; Yamazaki, K.; Shimoda, T. Direct Imprinting of Liquid Silicon. *ACS Appl. Mater. Interfaces* **2016**, 8, 9969–9976.
- (58) Iyer, G. R. S.; Hobbie, E. K.; Guruvenket, S.; Hoey, J. M.; Anderson, K. J.; Lovaasen, J.; Gette, C.; Schulz, D. L.; Swenson, O. F.; Elangovan, A.; Boudjouk, P. Solution-Based Synthesis of Crystalline Silicon from Liquid Silane through Laser and Chemical Annealing. ACS Appl. Mater. Interfaces 2012, 4, 2680–2685.

- (59) Lu, X.; Anderson, K. J.; Boudjouk, P.; Korgel, B. A. Low Temperature Colloidal Synthesis of Silicon Nanorods from Isotetrasilane, Neopentasilane, and Cyclohexasilane. *Chem. Mater.* **2015**, 27, 6053–6058.
- (60) Han, Y.; Anderson, K.; Hobbie, E. K.; Boudjouk, P.; Kilin, D. S. Unraveling Photodimerization of Cyclohexasilane from Molecular Dynamics Studies. *J. Phys. Chem. Lett.* **2018**, *9*, 4349–4354.
- (61) van Driel, A. F.; Nikolaev, I. S.; Vergeer, P.; Lodahl, P.; Vanmaekelbergh, D.; Vos, W. L. Statistical Analysis of Time-Resolved Emission from Ensembles of Semiconductor Quantum Dots: Interpretation of Exponential Decay Models. *Phys. Rev. B: Condens. Matter Mater. Phys.* **2007**, 75, 035329.
- (62) Huisken, F.; Ledoux, G.; Guillois, O.; Reynaud, C. Light-Emitting Silicon Nanocrystals from Laser Pyrolysis. *Adv. Mater.* **2002**, *14*, 1861–1865.
- (63) Miller, J. B.; Harris, J. M.; Hobbie, E. K. Purifying Colloidal Nanoparticles through Ultracentrifugation with Implications for Interfaces and Materials. *Langmuir* **2014**, *30*, 7936–7946.
- (64) Miller, J. B.; Hobbie, E. K. Nanoparticles as Macromolecules. J. Polym. Sci., Part B: Polym. Phys. 2013, 51, 1195–1208.
- (65) Mastronardi, M. L.; Hennrich, F.; Henderson, E. J.; Maier-Flaig, F.; Blum, C.; Reichenbach, J.; Lemmer, U.; Kübel, C.; Wang, D.; Kappes, M. M.; Ozin, G. A. Preparation of Monodisperse Silicon Nanocrystals Using Density Gradient Ultracentrifugation. *J. Am. Chem. Soc.* **2011**, *133*, 11928–11931.
- (66) Mangolini, L. Non-Thermal Plasma Synthesis and Passivation of Luminescent Silicon Nanocrystals, *Ph.D. Thesis*, University of Minnesota, Minneapolis, MN, 2007.
- (67) Schuck, P. Size-Distribution Analysis of Macromolecules by Sedimentation Velocity Ultracentrifugation and Lamm Equation Modeling. *Biophys. J.* **2000**, *78*, 1606–1619.
- (68) Schuck, P. Sedimentation Velocity Analytical Ultracentrifugation; CRC Press: Boca Raton, FL, 2016; pp 171–206.
- (69) Brown, P. H.; Balbo, A.; Zhao, H.; Ebel, C.; Schuck, P. Density Contrast Sedimentation Velocity for the Determination of Protein Partial-Specific Volumes. *PLoS One* **2011**, *6*, No. e26221.
- (70) Lees, E. E.; Gunzburg, M. J.; Nguyen, T. L.; Howlett, G. J.; Rothacker, J.; Nice, E.; Clayton, A. H. A.; Mulvaney, P. Experimental Determination of Quantum Dot Size Distributions, Ligand Packing Densities, and Bioconjugation Using Analytical Ultracentrifugation. *Nano Lett.* **2008**, *8*, 2883–2890.
- (71) Nontapot, K.; Rastogi, V.; Fagan, J. A.; Reipa, V. Size and Density Measurement of Core-Shell Si Nanoparticles by Analytical Ultracentrifugation. *Nanotechnology* **2013**, *24*, 155701.
- (72) Walter, J.; Gorbet, G.; Akdas, T.; Segets, D.; Demeler, B.; Peukert, W. 2D Analysis of Polydisperse Core-Shell Nanoparticles Using Analytical Ultracentrifugation. *Analyst* **2017**, *142*, 206–217.
- (73) Sykora, M.; Mangolini, L.; Schaller, R. D.; Kortshagen, U.; Jurbergs, D.; Klimov, V. I. Size-Dependent Intrinsic Radiative Decay Rates of Silicon Nanocrystals at Large Confinement Energies. *Phys. Rev. Lett.* **2008**, *100*, 6067401.
- (74) Boles, M. A.; Ling, D.; Hyeon, T.; Talapin, D. V. The Surface Science of Nanocrystals. *Nat. Mater.* **2016**, *15*, 141–153.
- (75) Giustino, F. Electron-Phonon Interactions from First Principles. *Rev. Mod. Phys.* **2017**, *89*, 015003.
- (76) Guruvenket, S.; Hoey, J. M.; Anderson, K. J.; Frohlich, M. T.; Krishnan, R.; Sivaguru, J.; Sibi, M. P.; Boudjouk, P. Synthesis of Silicon Quantum Dots Using Cyclohexasilane. *J. Mater. Chem. C* **2016**, *4*, 8206–8213.